





Liver injury monitoring using dynamic fluorescence molecular tomography based on a time-energy difference strategy

YIZHE ZHAO,^{1,2,†} SHUANGCHEN LI,^{1,2,†}  XUELEI HE,^{1,2,†} JINGJING YU,³  LIZHI ZHANG,^{1,2} HENG ZHANG,^{1,2} DE WEI,^{1,2} BEILEI WANG,^{1,2} JINTAO LI,^{1,2} HONGBO GUO,^{1,2,4}  AND XIAOWEI HE^{1,2,5} 

¹The Xi'an Key Laboratory of Radiomics and Intelligent Perception, Xi'an, China

²School of Information Sciences and Technology, Northwest University, Xi'an, 710127, China

³School of Physics and Information Technology, Shaanxi Normal University, Xi'an, 710062, China

⁴Guohb@nwnu.edu.cn

⁵hexw@nwnu.edu.cn

[†]These authors contributed equally to this work.

Abstract: Dynamic fluorescence molecular tomography (DFMT) is a promising molecular imaging technique that offers the potential to monitor fast kinetic behaviors within small animals in three dimensions. Early monitoring of liver disease requires the ability to distinguish and analyze normal and injured liver tissues. However, the inherent ill-posed nature of the problem and energy signal interference between the normal and injured liver regions limit the practical application of liver injury monitoring. In this study, we propose a novel strategy based on time and energy, leveraging the temporal correlation in fluorescence molecular imaging (FMI) sequences and the metabolic differences between normal and injured liver tissue. Additionally, considering fluorescence signal distribution disparity between the injured and normal regions, we designed a universal Golden Ratio Primal-Dual Algorithm (GRPDA) to reconstruct both the normal and injured liver regions. Numerical simulation and *in vivo* experiment results demonstrate that the proposed strategy can effectively avoid signal interference between liver and liver injury energy and lead to significant improvements in morphology recovery and positioning accuracy compared to existing approaches. Our research presents a new perspective on distinguishing normal and injured liver tissues for early liver injury monitoring.

© 2023 Optica Publishing Group under the terms of the [Optica Open Access Publishing Agreement](#)

1. Introduction

Liver cancer is the fourth most common cause of cancer-related death worldwide and imposes a heavy disease burden on humanity [1]. Clinical studies have demonstrated that liver injury serves as an initial stage of liver cancer and is the most common identifiable cause of acute liver failure. Therefore, early monitoring of liver injury regions plays a crucial role in the diagnosis and treatment of liver cancer [2]. Currently, several imaging techniques, including transient or shear-wave elastography, perfusion or dual-energy computed tomography, and contrast-enhanced magnetic resonance imaging [3], are employed in clinical practice to monitor liver injury [4]. However, limitations such as low repeatability, inaccurate imaging, radiation exposure, and requirement of specialized equipment severely hinder the practical application of these imaging techniques [5]. Conversely, fluorescence imaging/tomography has garnered considerable attention for liver injury monitoring and evaluation owing to its excellent performance, non-radiation exposure, high sensitivity, high specificity, and cost-effectiveness [6]. In particular, dynamic fluorescence molecular tomography (DFMT) provides a new potential approach for monitoring liver injury by imaging the temporal distributions of fluorescent probes and real-time quantitative

analyses of the different metabolic properties of the fluorescence agent in normal and injured liver at the cellular and molecular levels [7–9].

As an application extension of FMT, DFMT employs efficient source reconstruction methods to recover the distributions of fluorophore concentrations at different time points. Integrating pharmacokinetics and analytical methods with DFMT is a suitable approach that can aid in *in vivo* analyzing, predicting, and monitoring liver cancer. Over several decades, DFMT has established a solid foundation in imaging theories and algorithms, benefiting from the advancements made in FMT. Several FMT-based methods that use photon propagation models and inverse reconstruction algorithms can be directly applied to DFMT. The radiation transport equation (RTE) is an ideal photon propagation model that can theoretically describe light propagation in turbid media in DFMT [10]. However, due to its high computational costs, simplified models, such as diffusion equation theory (DE) [11], spherical harmonics (SPN) method, and hybrid models are commonly employed to solve the approximate problem [12]. In terms of inverse reconstruction, numerous effective regularization methods have been proposed for recovering the distributions of fluorophore concentrations [13] by considering the ill-posed nature of the inverse problem caused by the strong scattering property of biological tissues. Different probability distribution models are used for analyzing the measured noise, and typically, L_2 -norm (Tikhonov method) [14], L_1 -norm (Lasso method) [15], and L_p -norm ($0 < p < 1$) (non-convex method) [16] regularization. These extensive studies on theories and algorithms have significantly contributed to enhancing the accuracy and efficiency of FMT and have laid a solid theoretical foundation for DFMT.

Furthermore, with the development of imaging systems and dynamic fluorescent data acquisition strategies, DFMT has been utilized to resolve kinetic behaviors and dynamic physiological processes. In a hybrid FMT and X-ray computed tomography (XCT) system, the imaged object is continuously rotated to capture multiple circles of images, enabling the investigation of the pharmacokinetic rate of indocyanine green (ICG) in mouse liver [17]. To perform pharmacokinetics analyses using dynamic diffuse fluorescence tomography (DFT), a fiber-based dynamic DFT system was previously proposed for acquiring ICG tomographic image sequences using a square-wave modulation lock-in photocounting scheme and series-parallel measurement mode [18,19]. These imaging systems exhibit high sensitivity, high anti-ambient light ability, and cost-effectiveness. In addition, various methods have been explored for dynamic data processing. Recovered charge-coupled device (CCD) response curves are used in high-dynamic-range FMT (HDR-FMT), which are based on the multiple-exposure scheme, to enhance the dynamic range of FMT projection images [20]. Additionally, Liu et al. proposed a new assembling method by re-assembling the projections from two nearby circle scans while eliminating the temporal correlations within the fluorescence projection sequence [17]. These proposed dynamic data processing methods enhance the reconstruction quality and reduce the frame and reconstruction intervals in dynamic FMT imaging. Further, the frame-by-frame reconstruction approach and spatial-temporal image reconstruction methods are commonly used for image reconstruction in DFMT. Typically, in DFMT, images are obtained by independently and sequentially reconstructing the frames of a time sequence [7]. Although this method is straightforward and simple, it neglects the temporal correlations in the measured data, resulting in poor reconstruction quality and a reduced signal-to-noise ratio (SNR) [21,22]. To address this limitation, Liu et al. proposed an independent component analysis (ICA)-based method for dynamic fluorescence diffuse optical tomography (D-FDOT) imaging. This approach is suitable for imaging functional structures with different kinetic behaviors and provides associated time-course datasets [23]. Additionally, spatial-temporal image reconstruction methods, in which the reconstruction process of fluorescence concentrations is integrated with dynamic compartment models into a single step, have been proposed. These methods leverage the inherent temporal correlations in dynamic near-infrared (NIR) measurements and incorporate spatial-temporal a priori information into pharmacokinetic-rate images, enabling the imaging of pharmacokinetic parameters in small

animal organs [24]. These advanced technologies effectively improve the reconstruction quality and localization accuracy of fluorescent targets with large concentration differences, enabling the *in vivo* resolution of fast kinetic behaviors within small animals.

However, most previous studies on DFMT focus on pharmacokinetic parametric imaging. In the context of liver injury monitoring, it is focused on improving the low spatial resolution, which is caused by the inherent ill-posed nature of the problem, and overcoming signal interference between the liver and injured region remain challenging. To effectively distinguish normal and injured tissues in liver and monitor liver injuries from an early stage, we propose a difference strategy based on time and energy, aiming to accurately reconstruct the normal liver tissue and injured region. Firstly, considering the temporal correlation of sequence FMI, we propose a reconstruction strategy based on time difference, which effectively overcomes the interference between signals from the injured and normal regions, allowing accurate morphological recovery of the liver. Secondly, taking into account the differences between the metabolic characteristics of normal and injured liver in biological tissues [7,25], an energy difference strategy is employed to reconstruct the injured liver region. By considering the distinct distribution of fluorescence signals between the injured and normal regions, we developed a universal golden ratio primal-dual algorithm (GRPDA), which solves two distinct optimization models. Using this proposed algorithm, we can recover the morphologies of the liver and sparse injured region. To validate the effectiveness of the proposed time-energy difference strategy (T-EDS), both simulation and *in vivo* experiments were conducted. These experiments demonstrated that both normal and injured liver tissues can be clearly reconstructed using the proposed T-EDS; the reconstructed energy changes were consistent with the metabolic laws, and the method exhibited few artifacts while achieving a high degree of morphological recovery. Furthermore, the imaging results were verified *in vivo* by comparing with the vitro anatomy, further validating the effectiveness of the difference strategy.

2. Materials and methods

2.1. DFMT inverse reconstruction model

For the DFMT, coupled Diffusion Equations (DEs) are used to describe the light propagation in the forward problem [11], as shown in Eq. (1).

$$\begin{cases} \nabla \cdot [D_x(r)\nabla\Phi_x(r,t)] - \mu_{ax}(r)\Phi_x(r,t) = -\Theta\delta(r-r_s,t) & (r \in \Omega) \\ \nabla \cdot [D_m(r)\nabla\Phi_m(r,t)] - \mu_{am}(r)\Phi_m(r,t) = -\Phi_x(r)\eta\mu_{af}(r,t) & (r \in \Omega) \end{cases} \quad (1)$$

where Ω and $\delta(r)$ represent imaging region and the Dirac function, respectively, and Θ is a calibration factor, which accounts for the unknown gain of the FMT system. The subscripts x and m indicate the excited and emitted progressing, respectively. $\eta\mu_{af}(r,t)$ represents the unknown fluorescence yield distribution to be reconstructed. According to the finite element discretization [26], the coupling equations defined in Eq. (1) can be formulated as

$$AX(t) = B_t \quad (2)$$

where A is the system matrix determined by the optical properties of the excitation and emission process, $X(t)$ denotes the unknown internal distribution of the probes, and B_t represents the measurements of surface photon distribution.

In the DFMT, the system matrix A represents the relationship between the fluorescence distribution and measured surface photon distribution. During the light propagation progress, it remains stable at each time point. However, during the data acquisition process, the surface photon distribution B varies over time due to factors such as changes of the fluorophore concentration or

position of the fluorescence source. Based on the above objective analysis, the linear model for DFMT is formulated as

$$A [X(t_1), \dots, X(t_k)] = [B_1, \dots, B_k]^T \quad (3)$$

where $t_k = (1, \dots, K)$ represents the time point, and $X(t_k)$ is the unknown internal distribution of the probe at the k -th time point.

2.2. Time-energy difference strategy for Liver injury monitoring

The proposed method focuses on monitoring liver injury. This study applied it to both normal and injured tissue present in mouse liver. Considering the isotropic transport characteristic of light in the liver, the concentration of fluorophore is defined as a linear combination of the concentration distributions in the liver region and injury region.

$$X(t_k) = X_{\text{liver}}(t_k) + X_{\text{injure}}(t_k) \quad (4)$$

Furthermore, the measured signal is considered as a combination of the signal produced by the specific probe in the normal and injured tissue. According to the linear model of DFMT defined in Eq. (3), the combined measurement of the surface signal is as follows:

$$B(t_k) = B_{\text{liver}}(t_k) + B_{\text{injure}}(t_k) = A [X_{\text{liver}}(t_k) + X_{\text{injure}}(t_k)] \quad (5)$$

During the metabolism of ICG in mice, the time-varying fluorophore concentration $X(t_k)$ caused by metabolism of normal and injured liver tissue is described by a bi-exponential model using compartmental modeling. The regions of the liver and liver injury concentration distributions at time t are defined as follows:

$$X = -A(r) \exp(-\alpha(r)t) + B(r) \exp(-\beta(r)t) \quad (6)$$

where the parameters $A(r)$, $B(r)$, $\alpha(r)$ and $\beta(r)$ are pharmacokinetic parameters describing the uptake and release of fluorophores [24]. Both drug-induced and disease-oriented liver injury result in a slower metabolization rate of organismal organs compared to the normal case [27]. Thus, the uptake of fluorophore and uptake rate of liver $\alpha(r)_{\text{liver}}$ are greater than that of liver injury $\alpha(r)_{\text{injury}}$. Moreover, during the fluorophore excretion, the excretion rate of liver $\beta(r)_{\text{liver}}$ is greater than that of liver injury $\beta(r)_{\text{injury}}$ [7,24]. Based on the above analysis of the metabolic characteristics of liver and liver injury, partial derivatives of both sides of Eq. (5) with respect to t are defined as

$$A \left[\frac{\partial X_{\text{liver}}(t_k)}{\partial t_k} + \frac{\partial X_{\text{injure}}(t_k)}{\partial t_k} \right] = \left[\frac{\partial B_{\text{liver}}(t_k)}{\partial t_k} + \frac{\partial B_{\text{injure}}(t_k)}{\partial t_k} \right] \quad (7)$$

2.2.1. Liver reconstruction based on time difference

To mitigate the interference noise of the signals from the injured region on the liver, a time difference reconstruction strategy is proposed based on the following assumptions. During the whole metabolic process of fluorophore in liver, the metabolic rate of liver is higher than that in liver injury. Additionally, the normal region of liver is much larger than the injured region. Consequently, the metabolic process is predominantly governed by the normal liver cells, and changes in the time interval between consecutive frames in the region of liver injury can be disregarded. According to the above illustrations, the rate of change in liver metabolism is much higher than that in liver injury, i.e., $\frac{\partial X_{\text{liver}}(t_k)}{\partial t_k} \gg \frac{\partial X_{\text{injure}}(t_k)}{\partial t_k}$. Therefore, the change in liver injury is

ignored. As a result, Eq. (7) can be re-written as

$$A \frac{\partial X_{\text{liver}}(t_k)}{\partial t_k} = \frac{\partial B_{\text{liver}}(t_k)}{\partial t_k} \quad (8)$$

Considering the morphological recovery and extensive target reconstruction of liver, the objective function of Eq. (8) is solved by the reweighted L_2 -norm regulation method [28]:

$$\operatorname{argmin}_{i=1,\dots,k} \frac{1}{2} \left\| A \left(\frac{\partial X}{\partial t} \right)_{\text{liver}} - \left(\frac{\partial B}{\partial t} \right)_{\text{liver}} \right\|_2^2 + \lambda_{\text{liver}} \left(\frac{\partial X}{\partial t} \right)_{\text{liver}}^T L \left(\frac{\partial X}{\partial t} \right)_{\text{liver}} \quad (9)$$

where L is a structural prior obtained from the distance between nodes [29].

2.2.2. Liver region monitoring based on energy difference

As mentioned above, according to the compartmental model of the normal liver, when the derivative of Eq. (6) is 0 with respect to the liver, we can determine a time that satisfies the criteria $t_0 = \frac{1}{\beta-\alpha} \ln \frac{B\beta}{A\alpha}$, with the highest point of metabolic concentration being X_{max} . Therefore, before and after t_0 , there are two moments t_1 and t_2 that satisfy the condition: $X_{\text{liver}}(t_1) = X_{\text{liver}}(t_2)$. As the energy of the liver changes faster than that of the injured region, the energy of the injured region varies at different times, i.e., $X_{\text{injury}}(t_1) \neq X_{\text{injury}}(t_2)$. Therefore, the difference of the measured data at time t_1 and t_2 mainly reflects the different fluorescence agent metabolism distribution of the injury region, which satisfies

$$A(X_{t_2} - X_{t_1}) \approx A(\Delta X_k)_{\text{injury}} = B_{t_2} - B_{t_1} = \Delta B \quad (10)$$

According to the above equations and considering the sparse distribution of the injury region, Eq. (10) can be solved by the L_1 -norm regulation based algorithm as follows:

$$\operatorname{argmin} \frac{1}{2} \|A(\Delta X_k)_{\text{injury}} - \Delta B_{(t_2-t_1)}\|_2^2 + \lambda_{\text{injury}} \|(\Delta X_k)_{\text{injury}}\|_1 \quad (11)$$

2.2.3. GRPDA

To achieve three-dimensional reconstruction of both the normal and injury regions, we propose a general GRPDA based on the classical primal-dual algorithm (PDA) and incorporate all of its advantages. Within the framework of the GRPDA, two different objective functions (Eqs. (9) and (11)) are defined as follows:

$$\operatorname{argmin} F(Af) + R(f) \quad (12)$$

where:

$$F(Af) = \frac{1}{2} \|Af - g\|_2^2 \quad (13)$$

$$f = \begin{cases} (\Delta X_k)_{\text{injury}} & \text{(for Eq.9)} \\ (\Delta X_k)_{\text{liver}} & \text{(for Eq.11)} \end{cases} \quad (14)$$

$$g = \begin{cases} \Delta B_{(t_2-t_1)} & \text{(for Eq.9)} \\ \Delta B & \text{(for Eq.11)} \end{cases} \quad (15)$$

$$R = \begin{cases} \lambda_{\text{injury}} \left\| \sum_{k=t_1}^{t_2} (\Delta X_k)_{\text{injury}} \right\|_1 & \text{(for Eq.9)} \\ \lambda_{\text{liver}} (\Delta X_k)^T L (\Delta X_k) & \text{(for Eq.11)} \end{cases} \quad (16)$$

The saddle point, or primal-dual form of Eq. (12), is

$$\min_{f \in R^q} \max_{y \in R^q} \mathcal{L}(f, y) := R(f) + \langle Af, y \rangle - F^*(y) \quad (17)$$

where y is the coefficient of the Lagrange multiplier term, and F^* is the Legendre-Fenchel conjugate of F [30]. Using the convex combination technique [31], the specific expression of GRPDA with fixed step sizes $\tau = \frac{\sqrt{\psi}}{\sqrt{\beta E}}$, $\sigma = \beta\tau$ and golden ratio $\psi = 1.618$ is employed to obtain the optimal solution of Eq. (12). Moreover, the step size ratio $\beta = \sigma/\tau$ was set as 400 based on numerical experience. E is the eigenvalue of the system matrix A . The iterative solution process can be broken down into three steps:

$$\begin{cases} z_n = \frac{\psi-1}{\psi} f_{n-1} + \frac{1}{\psi} z_{n-1}, & z_0 = 0 \\ f_n = \text{prox}_{\tau R}(f_{n-1} - \tau A^T y_{n-1}), & f_0 = 0 \\ y_n = \text{prox}_{\sigma F^*}(y_{n-1} + \sigma A f_n), & y_0 = -g \end{cases} \quad (18)$$

3. Experimental settings

3.1. Numerical simulation

In the numerical simulations, a 3D digital mouse torso atlas with a height of 35 mm was employed [32], as shown in Fig. 1(a). The 3D digital mouse was divided into muscle, heart, liver, liver injury, stomach, kidneys, and lungs with specific optical parameters [7,32]. In Fig. 1(b), an irregular shape with a center of (12 mm, 12 mm, 16 mm) represents the liver injury region. The excitation points, represented by the blue dots, are located one transport mean free path beneath the surface on the plane. The fluorescence was measured from the opposite side, within a 150° field of view at Z=16 mm. Fig. 1(e) presents the ICG concentration curves, which simulate various metabolic processes of ICG in the liver and liver injury regions over a period of 200 minutes. These ICG curves were generated based on Eq. (6) using the corresponding pharmacokinetic parameters referenced from [7].

According to the liver metabolism, this study selected five time points ($t_1=0.6$ min, $t_2=10$ min, $t_3=14$ min, $t_4=57.5$ min, and $t_5=160$ min, corresponding to initial period, absorption stage, metabolic peak, half-life time, and excretion stage, respectively [33]) to display the reconstruction results. Firstly, to evaluate the feasibility of time difference strategy (T-DS) for recovering normal liver morphology, the traditional reconstruction framework without using any strategy was adopted for comparison [34]. To recovery the liver, the L_2 -norm form of GRPDA (GRPDA- L_2) was employed. In these experiments, DICE was used to evaluate the performance. Secondly, the energy difference strategy (E-DS) was compared with the feasible region strategy to prove its feasibility. Considering the sparse distribution of injury, the liver injury region was reconstructed using the L_1 -norm form of GRPDA (GRPDA- L_1), and the location error (LE) was calculated for comparison [34]. Further validation of the feasibility of T-EDS was conducted by overlapping the reconstruction results of liver and liver injury. Thirdly, to verify the universality of our proposed T-EDS and its applicability across different algorithms, we conducted experiments using two classical algorithms as baselines: Tikhonov and incomplete variables truncated conjugate gradient (IVTCG), rather than the efficient GRPDA algorithm.

Finally, we designed three stability experiments: (1) To monitor early liver injury, we reduced the difference in metabolic rates between normal and injured liver to simulate mild liver injury. The ICG concentration curve of the metabolic process in the mild liver injury region is shown by the green curve in Fig. 1(e). Compared with the red curve, the difference between liver and liver injury metabolism is reduced. (2) We also considered a larger injury region to monitor liver injury regions of different shapes. In Fig. 1(c), the irregular shape with a center of (15 mm, 12

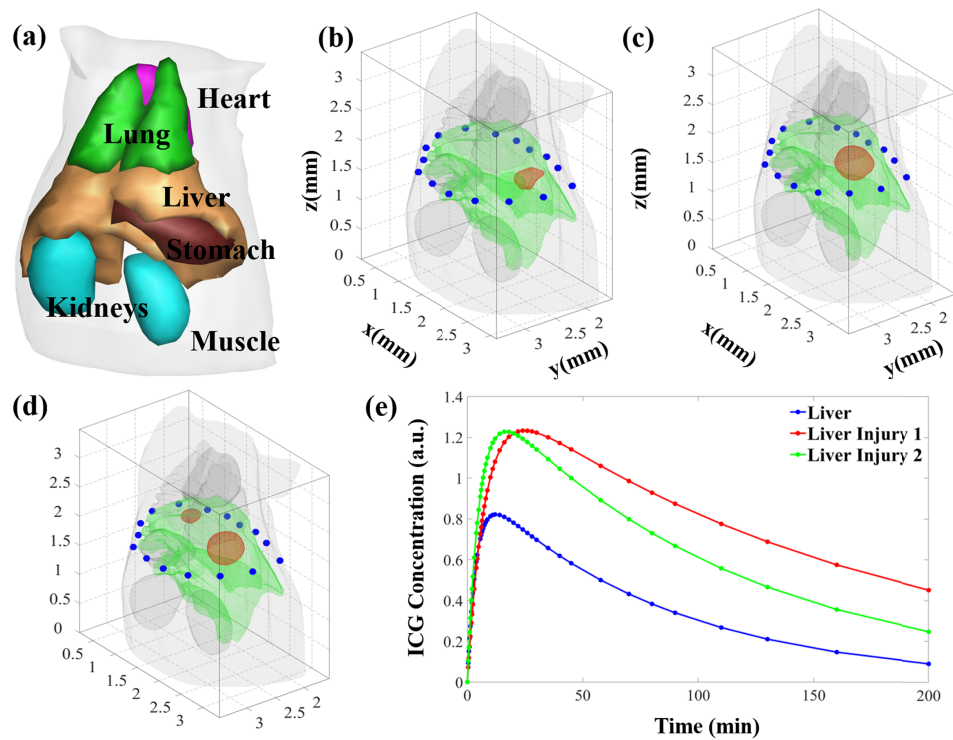


Fig. 1. Schematic diagram of the simulation model. (a) Torso of the mouse atlas model. (b)-(d) 3-D Digimouse model used for simulations. The blue points represent the excitation point source locations. (e) ICG concentration curves simulating the metabolic processes of ICG in liver and liver injury.

$mm, 16\text{ mm}$) represents a larger liver injury region. (3) We set up two injury regions with different sizes to monitor multiple liver injury regions. In Fig. 1(c), the two irregular shapes with centers of $(14\text{ mm}, 11\text{ mm}, 15.5\text{ mm})$ and $(23.5\text{ mm}, 12\text{ mm}, 14.5\text{ mm})$ represent two liver injury regions of different sizes.

3.2. *in vivo* experiment

The animal experiments conducted in this study complied with the ethical standards for animal welfare and were approved by the Animal Ethics Committee of the Northwest University of China. For the *in vivo* imaging experiments, a BKS-db mouse weighing approximately 35 g with fatty liver was fixed on the rotation stage of an integrated FMT/micro-CT system and anesthetized during the experiments. The excitation source was obtained by a continuous-wave semiconductor laser at 750 nm with a power of 450 mW, and fluorescence imaging was achieved using an 840 nm emission filter. A bolus of ICG (0.1 mL, 50 $\mu\text{g/mL}$) was injected into the tail vein before the fluorescent imaging. To ensure high-quality imaging, low exposure time (0.01 s), high shift speed (12.9 μs), and high-speed readout rate (10 MHz at 16-bit) were employed to restrain readout noise and shifting noise. During the acquisition process, the electron multiplying charge coupled device (EMCCD) camera was cooled to -80°C to reduce effects of thermal noise effects. Fluorescent images were captured continuously from the mouse at 6 seconds intervals for 20 hours to monitor the metabolic process of ICG in the liver. After the optical imaging, a hepatobiliary contrast agent (Fenestra LC) was slowly intravenously injected with a dosage of 15 mL/kg body weight through the abdominal cavity to enhance the anatomical structure of

the liver in micro-CT imaging. After 60 minutes of contrast agent injection, the mouse was immobilized and scanned using an X-ray source with a micro-focused cone beam (L9181-02, Hamamatsu Photonics, Hamamatsu Japan). In the X-ray scanning, the system was operated at a source voltage of 90 kV and power of 27 W. An X-ray flat-panel detector (C7942CA-22, Hamamatsu Photonics, Hamamatsu Japan), employed in high-resolution CT imaging, was used to obtain a total of 600 X-ray projections with an interval of 0.6° and integrating time of 0.5 seconds. The 3D anatomical structures were segmented from the CT data [35], and the major organs, including heart, lungs, liver, stomach, kidneys, and muscle, were segmented using Amria 5.2 (Amria, Visage Imaging, Australia), as shown in Fig. 2(a). Fig. 2(b) shows the energy signals collected within 20 hours, and the signal fitting results is depicted by the blue curve, reflecting the metabolic pattern of ICG in the mouse. Five representative frames at 6, 25, 138, 569, and 996 minutes were selected. Fig. 2(c) presents the corresponding fluorescence images captured by the CCD camera at these time points. Additionally, Fig. 2(d) illustrates the measured data mapped onto the 3D surface of the mouse torso.

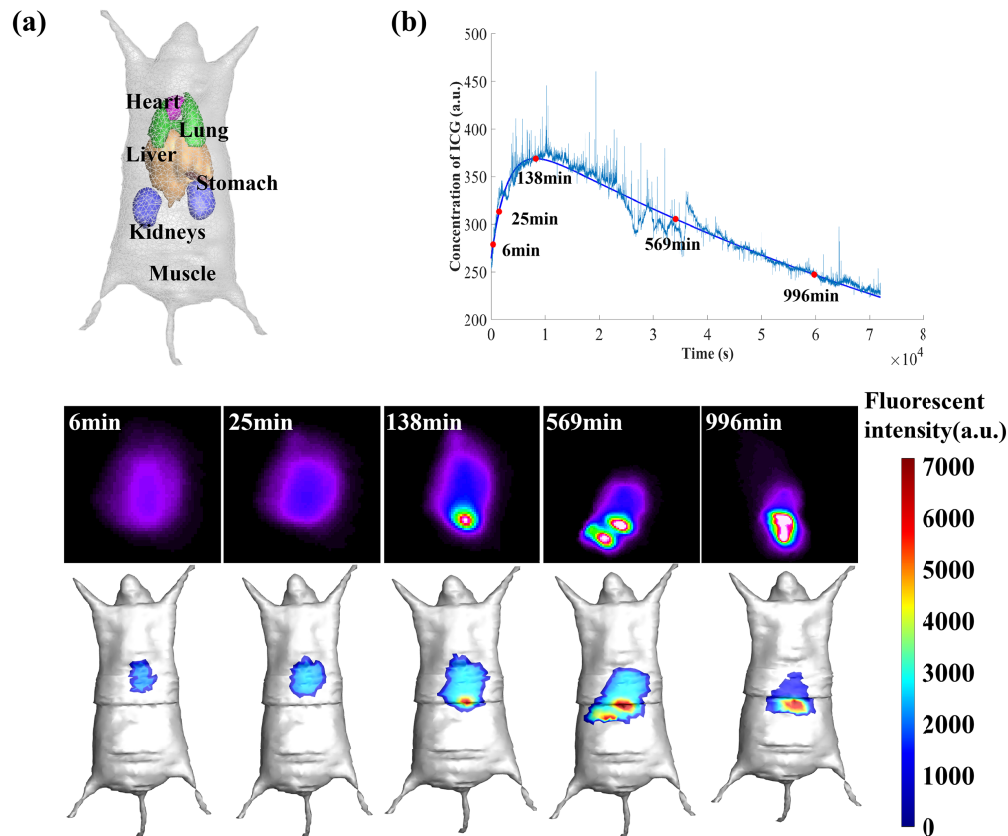


Fig. 2. Images of metabolism in mouse with fatty liver. (a) 3D anatomical structure segmentation from CT data. (b) Energy signals collected within 20 hours. (c) Fluorescent images of five representative frames. (d) Measurements mapped onto the 3D surface of the mouse torso.

4. Results

4.1. Simulation study

4.1.1. Liver reconstruction based on time difference

For comparing the liver morphology, the ground truth, reconstructed images of our proposed strategy, and traditional reconstruction images without T-DS are shown in Fig. 3(a1)-(a5), (b1)-(b5), and (c1)-(c5), respectively. Furthermore, DICE curves were plotted to evaluate the morphological recovery ability, as shown in Fig. 3(d). From Fig. 3(b1) - (b5), it can be observed that the liver contour is well-reconstructed at all five time points when using the T-DS, and the image quality is good, with minimal noise and closely resembling the ground truth. Moreover, the reconstructed energy changes follow the metabolic laws and are consistent with the real situation. Due to the presence of minor heterogeneity, the energy distribution was concentrated in the center of the liver. However, overall high morphological recovery ability was guaranteed. The DICE coefficient in Fig. 3(d) was approximately 0.78, which further demonstrates the high degree of morphological recovery achieved using the T-DS, reflecting the metabolic process of the probe in the liver over time.

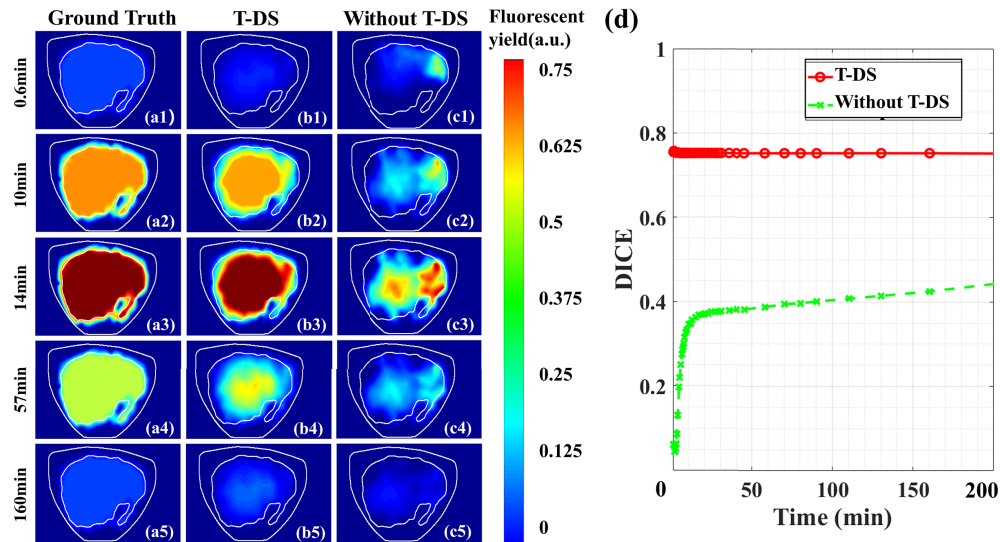


Fig. 3. Ground truth and reconstruction tomographic images of liver at five time points: (a1)-(a5) Ground truth of liver section corresponding to five time points. (b1)-(b5) Reconstruction results of five time points using T-DS. (c1)-(c5) Results of five time points without using T-DS. Moreover, in the transverse view, the white line indicates the actual positions of the contour of the digital mouse and contour of the mouse liver for the slice at $z=16\text{mm}$. (d) Curves of DICE obtained with and without the proposed T-DS for liver dynamic monitoring.

By contrast, the traditional reconstruction method, which is not based on the T-DS, can only approximately reconstruct the liver contour, as shown in Fig. 3(c1)-(c5). However, the reconstructed region exhibits a significant amount of discrete noise, leading to an uneven distribution of energy and poor continuity. The energy is predominantly concentrated in three regions near the center of the liver, with notably higher values observed at 14, 57, and 160 minutes. In addition, before the peak of the metabolic process, it was evident that the reconstruction results exhibit poor morphological recovery with significant loss of shape information, as shown in Fig. 3(c1) and (c2). The quantitative results in Fig. 3(d) further confirm the above statement, and the DICE of the reconstruction results are generally small, particularly in the first 20 minutes.

4.1.2. Liver region monitoring based on energy difference

Fig. 4 shows the ground truth, reconstructed images using our proposed E-DS, and traditional reconstruction results without using the E-DS at the corresponding five time points. Additionally, the LE curves of the reconstructed injured region compared to the ground truth are also shown in Fig. 4(d). These results obtained using the E-DS accurately capture the injured region at five time points and reflect the temporal changes in energy. In general, the quantitative results presented in Fig. 4(d) show that for 200 minutes of monitoring the injured liver region, the reconstruction results exhibit sparsity and achieve a satisfactory LE of 0.6066 mm, which is acceptable. Only minimal artifacts are observed, specifically at the half-life (57 minutes) and at 160 minutes.

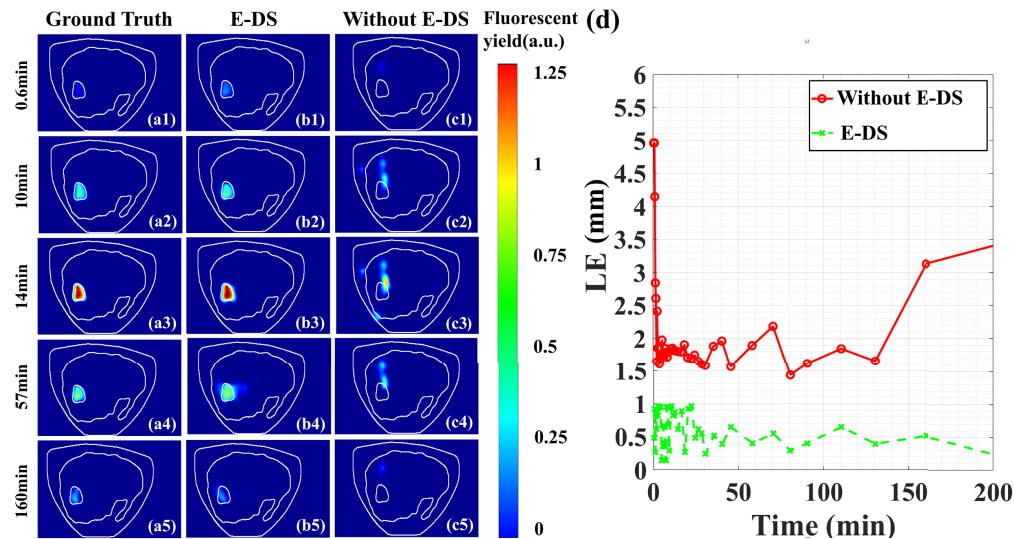


Fig. 4. Ground truth and reconstruction tomographic images of liver injury. (a1)-(a5) Ground truth of liver injury section corresponding to five time points. (b1)-(b5) Results of five time points using E-DS. (c1)-(c5) Results of five time points with feasible region strategy. (d) LE curves derived from the reconstruction results using E-DS and feasible region strategy in liver injury under dynamic monitoring.

In contrast, Fig. 4(c1)-(c5) demonstrate that the feasible region strategy only reflects the energy change trend over time without successfully reconstructing the liver injury region at these five time points. The reconstructed images show a considerable presence of artifacts and lack of sparsity. Moreover, there was a noticeable difference between the reconstructed and actual positions, particularly in the early and late stages of metabolism. The quantitative results in Fig. 4(d) further confirm the above statement. The LE of the feasible region strategy was greater than 1.5 mm at all time points, especially in the beginning and end stages of metabolism, with location errors reaching 5 mm and 3.5 mm, respectively.

4.1.3. Overlap between normal and injured liver regions

As shown in Figs. 3 and 4, we also overlapped the normal and injured liver region reconstruction results. Figs. 5(c1)-(c5) and 5(d1)-(d5) display the three-dimensional(3D) images and cross-sectional images (at $Z=16\text{mm}$) at five time points using the T-EDS, respectively. From the 3D view, the reconstruction results of T-EDS clearly differentiate between normal and injured liver regions, with the reconstructed energy confined within the liver contour. From the cross-sectional view, the reconstructed energy shows a slight unevenness and is slightly more concentrated at the center of the liver compared to the ground truth. In addition, the image is accompanied by a

small number of artifacts at the half-life (57 minutes). In contrast, Figs. 5(e1)-(e5) and 5(f1)-(f5) show the 3D and cross-sectional overlapping images obtained at five time points without using the T-EDS (at $Z=16\text{ mm}$). From the 3D view, the reconstructed energy is mainly concentrated in three regions near the center of the liver, showing uneven energy distribution and poor continuity. However, the normal and injured liver regions cannot be distinguished due to mutual interference between the signals from the cross-sectional and 3D images. In summary, the proposed T-EDS can effectively distinguishing between normal and injured liver regions and accurately reflect the different metabolic characteristics of the probes injected into the normal and injured parts of the liver. These features are beneficial for clinical applications of this method.

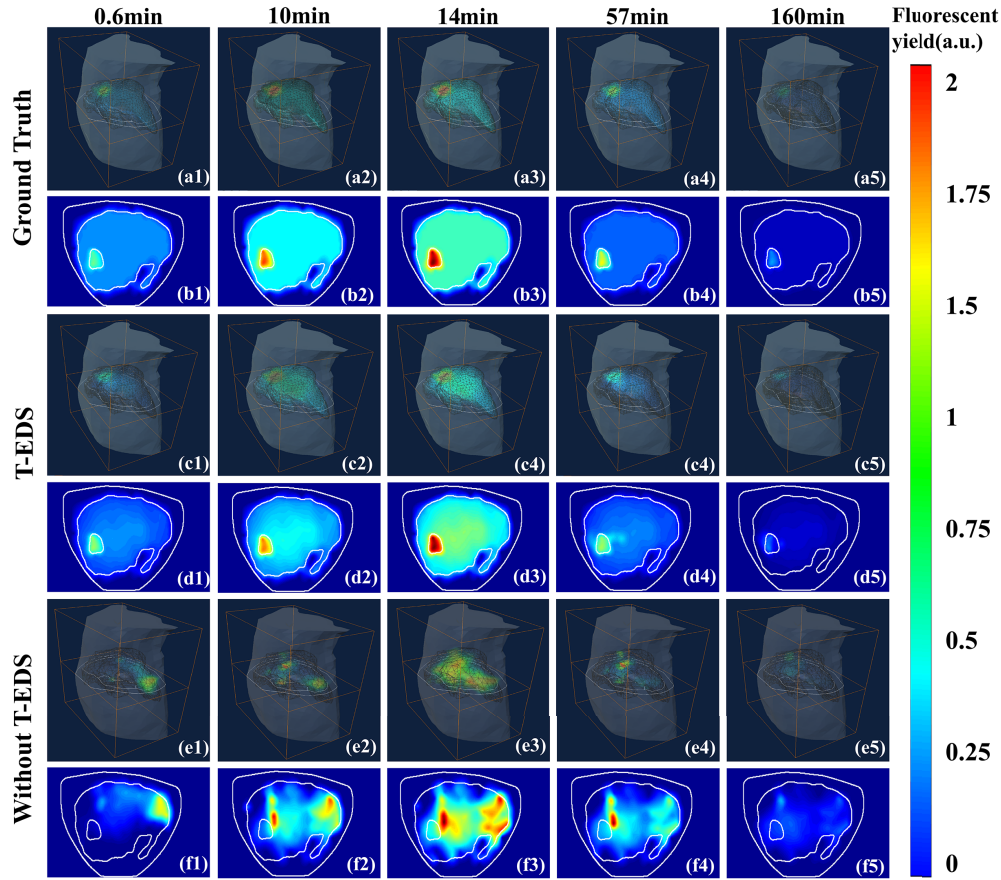


Fig. 5. Ground truth and reconstruction results by GRPDA at five time points. (a1)-(a5) Ground truth of 3D images. (b1)-(b5) Ground truth of cross-sectional images. (c1)-(c5) 3D images of the reconstruction results with T-EDS. (d1)-(d5) Cross-sectional images of the reconstruction results with T-EDS. (e1)-(e5) 3D images of the reconstruction results without T-EDS. (f1)-(f5) Cross-sectional images of the reconstruction results without T-EDS.

4.1.4. Robustness experiments

In method section and previous simulations, the proposed GRPDA can be applied to reconstruct the normal and injured regions simultaneously. To verify the universality of our proposed T-EDS, we replaced the GRPDA- L_2 algorithm with Tikhonov for liver recovery based on T-DS. Besides that, the IVTCG based on the L_1 -norm was adopted to reconstruct the injured region using the E-DS. For quantitative comparison, only the liver and liver injury reconstruction results

at the metabolic peak are depicted in 3D and cross-sectional views (at $Z=16\text{ mm}$), as shown in Fig. 6(a1)-(a5) and Fig. 6(b1)-(b5), respectively. The intensity distribution curves along the x , y , and z -axes, passing through the center of the injury region (12 mm , 12 mm , 16 mm), are depicted in Fig. 6(c), (d), and (e), respectively. It was observed that the T-EDS based on different reconstruction algorithms can clearly reconstruct the normal and injured regions, producing acceptable results that indicate the robustness of the proposed strategy. Specifically, from Fig. 6 (b2, b4) and (b3, b5), it can be concluded that the reconstructed liver through GRPDA-L2 shows better morphological recovery ability than Tikhonov. Moreover, it is evident that GRPDA-L1 exhibits higher positioning accuracy than IVTCG in reconstructing the liver injury region. From the perspectives of Fig. 6 (b2,b3), it more closely resembles the ground truth than that of Fig. 6 (b4,b5). Moreover, the liver-injury monitoring performance of the combination of GRPDA-L2+GRPDA-L1 surpasses those of the other three combinations. Conversely, the combination of Tikhonov+IVTCG produced the worst results among the four combinations. These above conclusions can also be confirmed from Fig. 6(c)-(e). From the ground truth (black line in the figure), the peak and plateau regions represent the injured and normal liver regions, respectively. The tendency of the red dashed line is closely aligned with the black curve in both the peak and plateau regions, while the peak region of IVTCG and plateau region of Tikhonov show the slight positional deviation along the x , y and z -axes. In summary, the comparison results highlight that the proposed T-EDS based on GRPDA can significantly improve the accuracy of reconstruction with a high morphological recovery ability and good robustness.

4.2. Stability experiments

Figure 7(a)-(i) show the 3D and cross-sectional images (at $Z=16\text{ mm}$) obtained at five time points using the T-EDS in three stability experiments. To further validate the reconstruction performance of our proposed strategy, we quantified the localization accuracy and morphology recovery performance using the LE and DICE indexes, as shown by the two box plots in Fig. 7(m) and Fig. 7(n), respectively. In the early stages of the injury, we observed that the sparse injured region can still be monitored, and the quantitative results are acceptable. However, compared to the case with significant metabolic differences, this scenario is more challenging, resulting in a slight decline, especially in the early (0.6 minutes) and late stages (160 minutes) of the metabolism, where the LE is 1.6 mm . Moreover, for the large liver injury region, apart from small artifacts at 0.6 minutes (Fig. 7(g1)), the reconstruction accuracy remains high throughout the entire 200 minutes of liver injury monitoring. Monitoring multiple injured regions in a liver is more challenging because of signal interference between the injured regions. However, the proposed strategy can clearly distinguish between two injured regions throughout the metabolic process, yielding a satisfactory result with an average DICE greater than 0.7. It is worth noting that the LE slightly increases because of deviations in the reconstructed intensity of the metabolism 10 minutes. Overall, our proposed T-EDS shows satisfactory stability and meets basic application requirements.

4.3. *in vivo* experiment results

In the *in vivo* experiment, CT/MRI imaging could not reveal the injured regions in the liver. Therefore, we performed dissected the liver as a standard procedure, as illustrated in Fig. 8(a). To validate the effectiveness of our proposed T-EDS, we utilized 2D photographs of the dissected liver, discrete point cloud data obtained from the CT images of the dissected liver, and the whole *in vivo* mouse for registration. Firstly, the blue circular dashed line in Fig. 8(a) represents the region of the fatty liver, characterized by a darker color compared to normal liver tissue. Important reference points around the injured regions are marked as a-e. Based on the 2D-3D radiological changes, five corresponding feature points are plotted on the 3D mesh of the dissected liver in Fig. 8(b). Finally, we conducted cloud point registration using the classical Iterative Closest

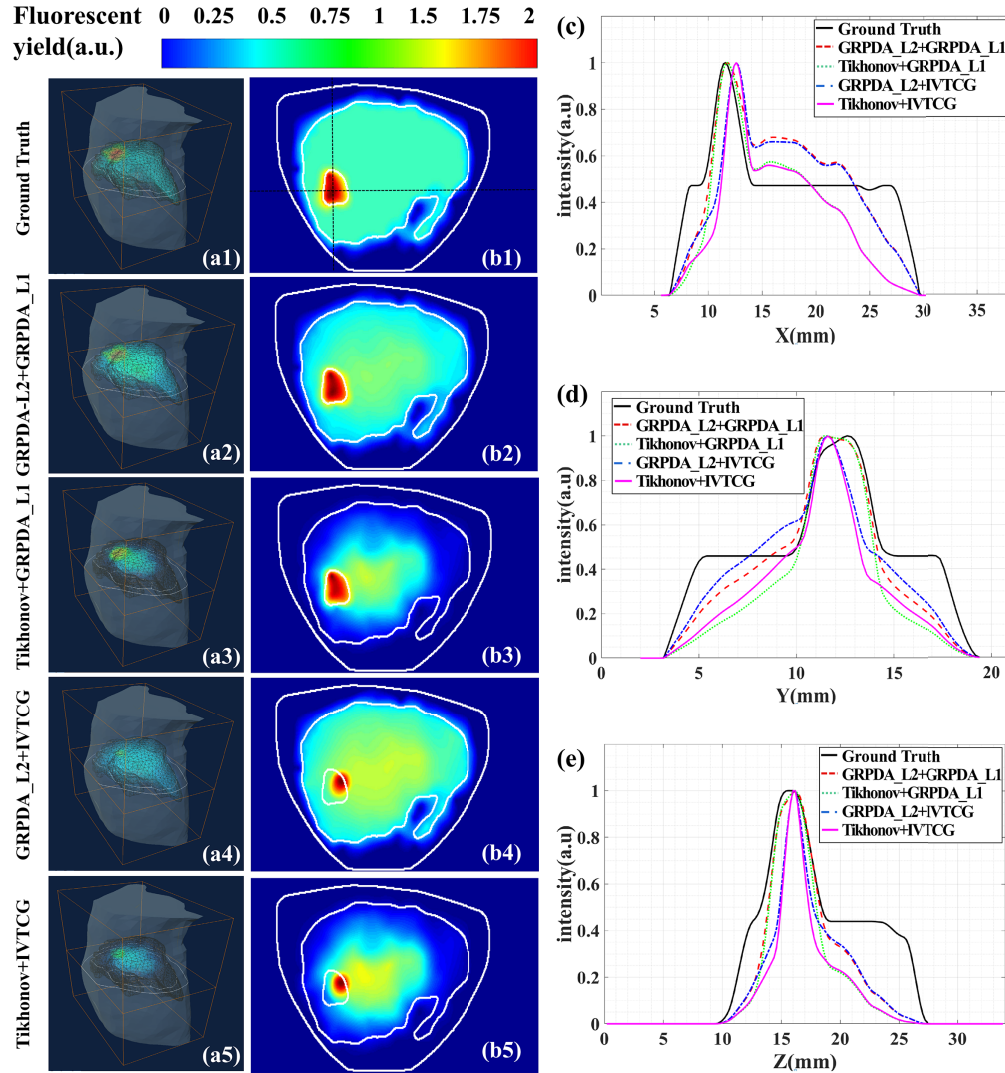


Fig. 6. Results of robustness experiments. (a1)-(a5) 3D images of ground truth and reconstructed results under different algorithm combinations. (b1)-(b5) Cross-sectional images of ground truth and reconstructed results under different algorithm combinations. (c-e) Intensity distribution of the ground truth and reconstruction results along x, y and z-axis.

Point approach to find the five important marker points on the 3D mesh of the whole *in vivo* mouse, as depicted in Fig. 8(c). These five reference points are also marked in Figs. 8(d) and (e) to evaluate the liver injury monitoring results. Figs. 8(d1) - (d5) demonstrate the reconstruction results obtained using the T-EDS at these five time points. The reconstructed ICG distribution is confined within the liver contour, and the ICG accumulated in the injury regions can be clearly distinguished from the hepatic ICG uptake. Moreover, the ICG concentration first increases and then decreases in accordance with the expected metabolic pattern. Furthermore, the reconstructed injury regions shown in red are all concentrated near the five marked points, without distribution in other positions, which is consistent with Fig. 8(a). Conversely, Figs. 8(e1)-(e5) show the results obtained without using the T-EDS and indicate that the reconstructed ICG distribution slightly extends beyond the liver contour. The injured regions are distributed around these five marked points as well as converge in the anterior surface of the liver, indicating a significant difference from the results shown in Fig. 8(a). These findings further highlight the significance and effectiveness of the proposed T-EDS in obtaining morphological information and accurately tracking the *in vivo* position of fluorescent probe distribution.

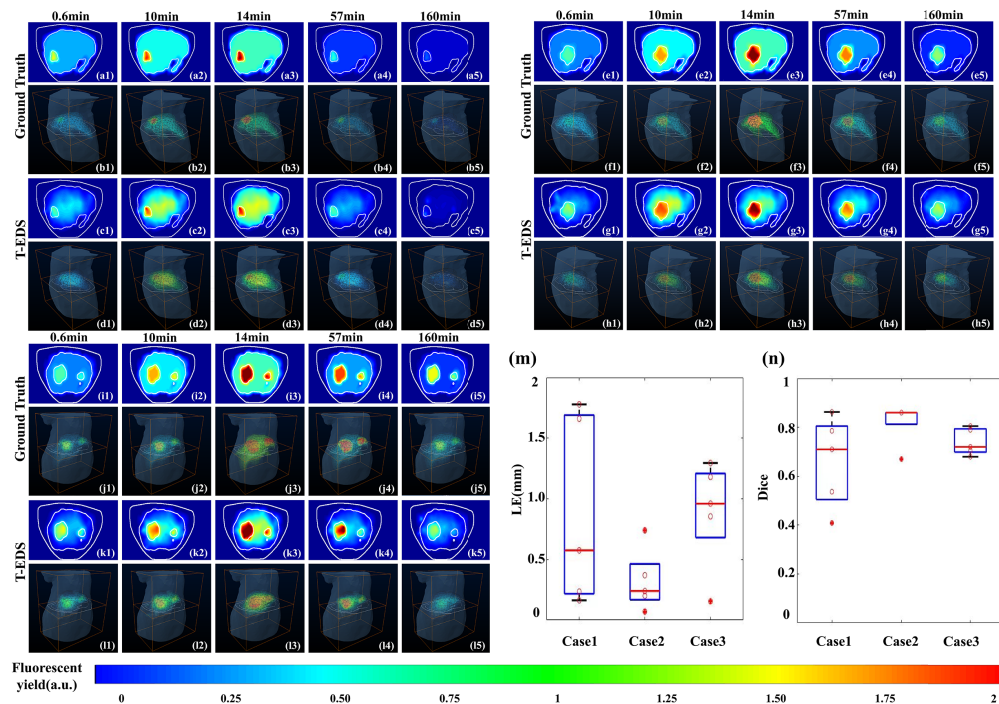


Fig. 7. 3D and cross-sectional images of the reconstructed results using the T-EDS in three stability experiments. (a)-(d), (e)-(h), and (i)-(l) represent the reconstructed results at five time points in the case of early liver injury, larger-sized injured region, and two injured regions, respectively. (m) and (n) are box plots of LE and DICE.

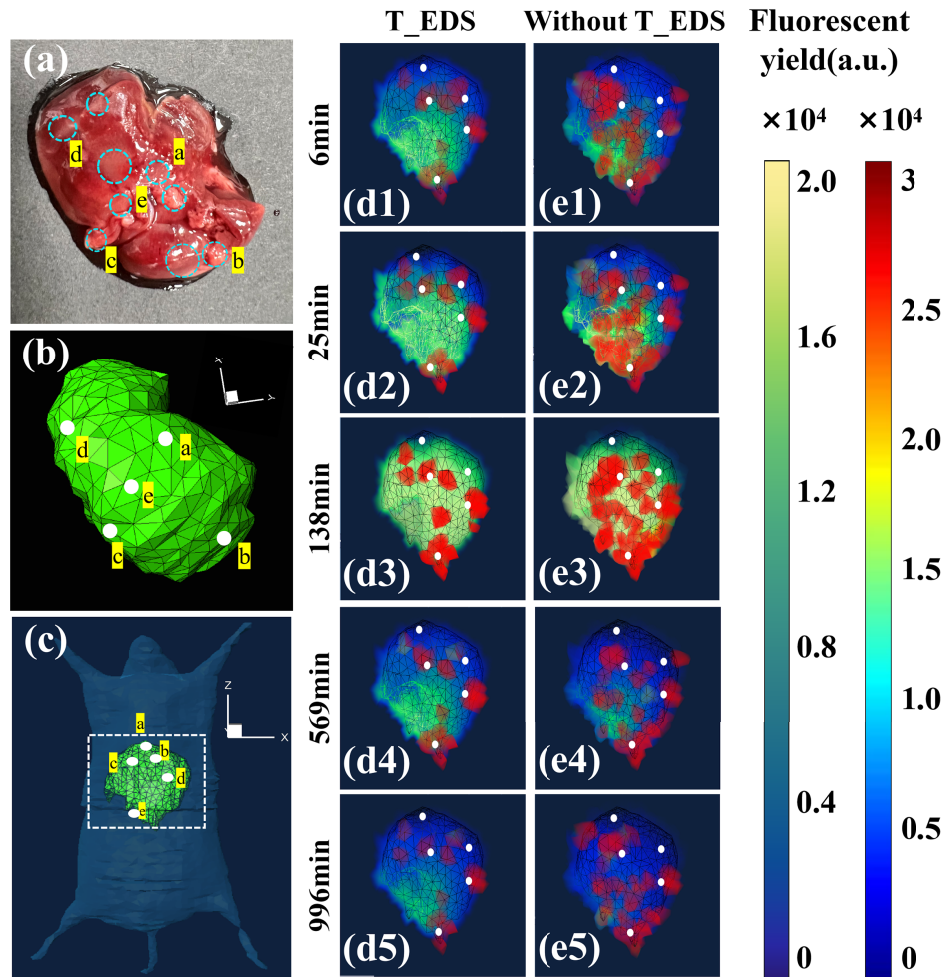


Fig. 8. Photograph, 3D images, and reconstructed results of fatty liver in the mouse after dissection. (a) Photograph of the fatty liver in the mouse after dissection. (b) 3D visualization corresponding to (a). (c) Visualization of fatty liver over the entire mouse. (d1)-(d5) Reconstruction results with T-EDS at five time points. (e1)-(e5) Reconstruction results without T-EDS at five time points.

5. Discussion and conclusion

As a promising preclinical imaging technique, DFMT has attracted considerable attention in the fields of imaging theory, acquisition equipment, and biomedical applications. However, due to the severe ill-posedness of inverse problems and the interference of signals between the injured region and normal liver, early liver injury monitoring using DFMT is still challenging in biological applications.

In this study, we proposed a novel difference strategy based on time and energy, which effectively distinguished between normal and injured tissues in mouse liver to achieve early liver injury monitoring. Firstly, we proposed the T-DS, which can effectively overcome the interference between signals from the injured region and normal liver and can recover the morphology of the liver. Then, considering the differences between the metabolic characteristics in the normal and injured liver tissues, an E-DS was employed to reconstruct the liver injury region. Moreover, considering the extensive target reconstruction of the liver and sparse distribution of the injured region, a universal GRPDA was employed to solve two distinct optimization models. This algorithm enabled the recovery of the morphologies of both the normal liver and sparse injured region.

The accuracy and stability were evaluated through numerical simulations. The results showed that the E-DS could significantly improve the degree of morphological recovery of liver, with an average DICE of 0.78 (see Fig. 4), and T-DS improved the accuracy of liver injury localization with a satisfactory LE of 0.6066 mm (seen in Fig. 5). Overall, high morphological recovery ability could be guaranteed, accurately capturing the liver injury region. Furthermore, the results of robustness experiments not only validated the applicability and generality of the proposed strategy with different reconstruction algorithms, but also demonstrated the superiority of GRPDA. Finally, three sets of stability experiments further validated the effectiveness of our proposed strategy in more challenging situations; these proposed strategy yielded satisfactory results and fulfilled basic application requirements. In the *in vivo* experiments, a fatty liver mouse model was developed to further validate the practicability of the proposed T-EDS. The *in vivo* results demonstrated that the proposed strategy could recover shape of the entire liver profile with a high accuracy, and the spatial resolution for detecting fatty liver tissues improved. It is important to note that our *in vivo* experiments did not involve accurate quantitative research on the distribution of fatty liver tissues. We recognize the significance of conducting such quantitative investigations in the future work by leveraging the advantages of other imaging modalities, such as magnetic particle imaging [36], positron emission tomography, and single photon emission computed tomography [37]. Besides that, some reliable contrast mechanisms, such as lifetime and FRET, were not used in our research. The proposed T-EDS was developed to distinguish normal and injured liver tissue geometrically, rather than to quantify the metabolic processes of the liver and injured regions, which is limited by imaging equipment and quantitative instruments. Our optical image device (EMCCD) cannot be used to compute the lifetime of the fluorescence probe. Therefore, further studies will be conducted to explore optical calibration techniques (such as the sphere integration method) to address this issue. In addition, quantitative research on cell/fluorescence signal/probe quantum yield and device upgrades will be conducted in the future.

We believe that the proposed strategy can provide a new perspective to distinguish normal and injured tissues in liver, enabling early liver injury monitoring. Further, it can broaden the applicability of DFMT in various preclinical processes and facilitate the theoretical development of optical molecular tomography.

Funding. National Natural Science Foundation of China, Grant/Award Numbers (11871321, 12271434, 61901374, 61906154, 61971350, 62201459, 62271394, 82071914).

Disclosures. The authors declare no potential conflict of interests.

Data availability. Data underlying the in-vivo results presented in this paper are not publicly available at this time but may be obtained from the authors upon reasonable request.

References

1. J. D. Yang, P. Hainaut, G. J. Gores, A. Amadou, A. Plymoth, and L. R. Roberts, "A global view of hepatocellular carcinoma: trends, risk, prevention and management," *Nat. Rev. Gastroenterol. Hepatol.* **16**(10), 589–604 (2019).
2. H. Rumgay, M. Arnold, J. Ferlay, O. Lesi, C. J. Cabasag, J. Vignat, M. Laversanne, K. A. McGlynn, and I. Soerjomataram, "Global burden of primary liver cancer in 2020 and predictions to 2040," *J. Hepatol.* **77**(6), 1598–1606 (2022).
3. L. Petittclerc, G. Sebastiani, G. Gilbert, G. Cloutier, and A. Tang, "Liver fibrosis: Review of current imaging and mri quantification techniques," *J. Magn. Reson. Imaging* **45**, 1276–1295 (2017).
4. J. M. Horowitz, S. K. Venkatesh, R. L. Ehman, K. Jhaveri, P. Kamath, M. A. Ohliger, A. E. Samir, A. C. Silva, B. Taouli, M. S. Torbenson, B. Michael L., and H. F. Miller, "Evaluation of hepatic fibrosis: a review from the society of abdominal radiology disease focus panel," *Abdom. Radiol.* **42**(8), 2037–2053 (2017).
5. J. A. Talwalkar, M. Yin, J. L. Fidler, S. O. Sanderson, P. S. Kamath, and R. L. Ehman, "Magnetic resonance imaging of hepatic fibrosis: emerging clinical applications," *Hepatology* **47**(1), 332–342 (2007).
6. P. Zhang, C. Ma, F. Song, G. Fan, Y. Sun, Y. Feng, X. Ma, F. Liu, and G. Zhang, "A review on imaging methodology advances in fluorescence molecular tomography," *Phys. Med. Biol.* **67**(10), 10TR01 (2022).
7. G. Zhang, F. Liu, H. Pu, W. He, J. Luo, and J. Bai, "A direct method with structural priors for imaging pharmacokinetic parameters in dynamic fluorescence molecular tomography," *IEEE Trans. Biomed. Eng.* **61**(3), 986–990 (2014).
8. M. L. James and S. S. Gambhir, "A molecular imaging primer: modalities, imaging agents, and applications," *Physiol. Rev.* **92**(2), 897–965 (2012).
9. B. Wang, S. Li, L. Zhang, J. Li, Y. Zhao, J. Yu, X. He, H. Guo, and X. He, "A review of methods for solving the optical molecular tomography," *J. Appl. Phys.* **133**(13), 130701 (2023).
10. R. Baiejiang, Y. Zhao, B. Z. Fite, K. W. Ferrara, and C. Li, "Anatomical image-guided fluorescence molecular tomography reconstruction using kernel method," *J. Biomed. Opt.* **22**(5), 055001 (2017).
11. L. V. Wang and H.-I. Wu, *Biomedical optics: principles and imaging* (John Wiley & Sons, 2012).
12. A. D. Klose and E. W. Larsen, "Light transport in biological tissue based on the simplified spherical harmonics equations," *J. Comput. Phys.* **220**(1), 441–470 (2006).
13. H. Zhang, X. He, J. Yu, X. He, H. Guo, and Y. Hou, "L1-l2 norm regularization via forward-backward splitting for fluorescence molecular tomography," *Biomed. Opt. Express* **12**(12), 7807–7825 (2021).
14. C. Qin, X. Yang, J. Feng, K. Liu, J. Liu, G. Yan, S. Zhu, M. Xu, and J. Tian, "Adaptive improved element free galerkin method for quasi-or multi-spectral bioluminescence tomography," *Opt. Express* **17**(24), 21925–21934 (2009).
15. X. He, J. Liang, X. Wang, J. Yu, X. Qu, X. Wang, Y. Hou, D. Chen, F. Liu, and J. Tian, "Sparse reconstruction for quantitative bioluminescence tomography based on the incomplete variables truncated conjugate gradient method," *Opt. Express* **18**(24), 24825–24841 (2010).
16. X. He, J. Yu, X. Wang, H. Yi, Y. Chen, X. Song, and X. He, "Half thresholding pursuit algorithm for fluorescence molecular tomography," *IEEE Trans. Biomed. Eng.* **66**(5), 1468–1476 (2019).
17. X. Liu, X. He, Z. Yan, and H. Lu, "4-d reconstruction of fluorescence molecular tomography using re-assembled measurement data," *Biomed. Opt. Express* **6**(6), 1963–1976 (2015).
18. G. Zhang, F. Liu, B. Zhang, Y. He, J. Luo, and J. Bai, "Imaging of pharmacokinetic rates of indocyanine green in mouse liver with a hybrid fluorescence molecular tomography/x-ray computed tomography system," *J. Biomed. Opt.* **18**(4), 040505 (2013).
19. L. Zhang, N. Cheng, H. Liu, Y. Pan, Y. Zhang, and F. Gao, "High-sensitivity dynamic diffuse fluorescence tomography system for fluorescence pharmacokinetics," *J. Biomed. Opt.* **27**(04), 046002 (2022).
20. L. Lian, Y. Deng, W. Xie, G. Xu, X. Yang, Z. Zhang, and Q. Luo, "High-dynamic-range fluorescence molecular tomography for imaging of fluorescent targets with large concentration differences," *Opt. Express* **24**(17), 19920–19933 (2016).
21. M. Gurfinkel, A. B. Thompson, W. Ralston, T. L. Troy, J. S. Reynolds, B. Muggenberger, K. Nikula, R. Pandey, R. Mayer, D. J. Hawrysz, and E. M. Seveck-Muraca, "Pharmacokinetics of icg and hpph-car for detection of normal and tumor tissue using fluorescence, near-infrared continuous wave imaging," in *Biomedical Optical Spectroscopy and Diagnostics*, (Optica Publishing Group, 2000), p. MD7.
22. K. O. Vasquez, C. Casavant, and J. D. Peterson, "Quantitative whole body biodistribution of fluorescent-labeled agents by non-invasive tomographic imaging," *PLoS One* **6**(6), e20594 (2011).
23. X. Liu, F. Liu, Y. Zhang, and J. Bai, "Unmixing dynamic fluorescence diffuse optical tomography images with independent component analysis," *IEEE Trans. Med. Imaging* **30**(9), 1591–1604 (2011).
24. G. Zhang, H. Pu, W. He, F. Liu, J. Luo, and J. Bai, "Full-direct method for imaging pharmacokinetic parameters in dynamic fluorescence molecular tomography," *Appl. Phys. Lett.* **106**(8), 081110 (2015).
25. F. Liu, P. Zhang, Z. Liu, F. Song, C. Ma, Y. Sun, Y. Feng, Y. He, and G. Zhang, "In vivo accurate detection of the liver tumor with pharmacokinetic parametric images from dynamic fluorescence molecular tomography," *J. Biomed. Opt.* **27**(07), 070501 (2022).
26. M. Schweiger, S. Arridge, M. Hiraoka, and D. Delpy, "The finite element method for the propagation of light in scattering media: boundary and source conditions," *Med. Phys.* **22**(11), 1779–1792 (1995).

27. S. C. Lu, H. Tsukamoto, and J. M. Mato, "Role of abnormal methionine metabolism in alcoholic liver injury," *Alcohol* **27**(3), 155–162 (2002).
28. H. Yi, D. Chen, W. Li, S. Zhu, X. Wang, J. Liang, and J. Tian, "Reconstruction algorithms based on l_1 -norm and l_2 -norm for two imaging models of fluorescence molecular tomography: a comparative study," *J. Biomed. Opt.* **18**(5), 056013 (2013).
29. X. He, H. Meng, X. He, K. Wang, X. Song, and J. Tian, "Nonconvex laplacian manifold joint method for morphological reconstruction of fluorescence molecular tomography," *Mol. Imaging Biol.* **23**(3), 394–406 (2021).
30. J. Côté, "A lagrange multiplier approach for the metric terms of semi-lagrangian models on the sphere," *Q. J. Royal Meteorol. Soc.* **114**, 1347–1352 (1988).
31. Y. Malitsky, "Golden ratio algorithms for variational inequalities," *Math. Program.* **184**(1-2), 383–410 (2020).
32. A. Ale, V. Ermolayev, E. Herzog, C. Cohrs, M. H. De Angelis, and V. Ntziachristos, "Fmt-xct: in vivo animal studies with hybrid fluorescence molecular tomography–x-ray computed tomography," *Nat. Methods* **9**(6), 615–620 (2012).
33. H. Shinohara, A. Tanaka, T. Kitai, N. Yanabu, T. Inomoto, S. Satoh, E. Hatano, Y. Yamaoka, and K. Hirao, "Direct measurement of hepatic indocyanine green clearance with near-infrared spectroscopy: separate evaluation of uptake and removal," *Hepatology* **23**, 137–144 (1996).
34. H. Meng, K. Wang, Y. Gao, Y. Jin, X. Ma, and J. Tian, "Adaptive gaussian weighted laplace prior regularization enables accurate morphological reconstruction in fluorescence molecular tomography," *IEEE Trans. Med. Imaging* **38**(12), 2726–2734 (2019).
35. B. Dogdas, D. Stout, A. F. Chatzioannou, and R. M. Leahy, "Digimouse: a 3d whole body mouse atlas from ct and cryosection data," *Phys. Med. Biol.* **52**(3), 577–587 (2007).
36. L. Yin, H. Guo, P. Zhang, Y. Li, H. Hui, Y. Du, and J. Tian, "System matrix recovery based on deep image prior in magnetic particle imaging," *Phys. Med. Biol.* **68**(3), 035006 (2023).
37. A. Rahmim and H. Zaidi, "Pet versus spect: strengths, limitations and challenges," *Nucl. Med. Commun.* **29**(3), 193–207 (2008).